Geometry of X-ray based measurement of residual strain at desired penetration depth

A. Morawiec

Polish Academy of Sciences, Institute of Metallurgy and Materials Science

Reymonta 25, 30–059 Kraków, Poland

E-mail: nmmorawi@cyf-kr.edu.pl   Tel.: ++48–122952854   Fax: ++48–122952804

Abstract

X-ray based measurement of residual lattice strains at chosen penetration depth is one of the methods for investigating strain inhomogeneities in near-surface layers of polycrystalline materials. The measurement relies on determining shifts of Bragg peaks for various directions of the scattering vector with respect to the specimen. At each of these directions, to reach a given the penetration depth, a proper specimen orientation is required. The task of determining such orientations, albeit elementary, is quite intricate. The existing literature describes only partial solutions with unspecified domains of application, which fail if applied to beyond the domains. Therefore, geometric aspects of the measurement are analyzed in details. Explicit bounds on measurement parameters are given. The equation fundamental for the procedure is solved with respect to specimen orientations. For a given direction of the scattering vector, there are generally four different specimen orientations leading to the same penetration depth. This simple fact (overlooked in previous analyzes) can be used for improving reliability of measurement results. Analytical formulas for goniometer angles representing these orientations are provided.

1. Introduction

Residual strains in polycrystalline materials are frequently measured using X-ray diffraction by recording shifts of Bragg diffraction peaks at various tilts of the specimen with respect to the X-ray beam [1]. Results of these measurements are affected by strain inhomogeneities. To investigate strain gradients along the normal to the specimen surface, methods accounting for X-ray penetration depth have been devised; for a review, see [2] and references therein. There is a large and growing interest in such methods due to the importance of materials with steep stress gradients, especially surface treated materials and polycrystalline coatings, e.g., [3–6]. As the penetration depth varies with the specimen tilt, special measurement geometries are used; the most basic techniques of this kind referred to as "χ mode" and "ω mode"[1] rely on simple relationships between the penetration depth and the tilt angles. An alternative approach is to measure strain at constant penetration depth, in the so-called "combined ω/χ mode" [2, 9, 10]. To perform such a measurement at a given Bragg angle, the remaining angles of a diffractometer need to be varied in a proper manner so the penetration depth remains unchanged. Therefore full understanding of the geometry of the measurement is required, and the technical issue of setting proper goniometer angles are of fundamental importance. Formulas for the angles of the standard four-circle diffractometer, a detailed strategy of the measurement, and descriptions of the method were published in [9–12]. However, the descriptions of the measurement geometry given in these article have deficiencies: they are incomplete with unspecified domains of application, and thus incorrect if applied beyond these domains. This paper completes these descriptions and presents a broader perspective on geometric aspects of the "combined ω/χ mode". It provides explicit bounds on measurement parameters and a full solution of the fundamental equation of the method with respect to specimen orientations. For a given direction of the scattering vector, up to four different specimen orientations lead to the same penetration depth. Knowing these orientations will be useful for confirming measurement data (by comparing peak positions from different configurations), or generally, for getting more reliable results. The possibility of measuring lattice strains at the same penetration depth in four specimen orientations has not been recognized before. These four orientations are characterized. In particular, analytical formulas for all goniometer angles for each of these orientations are given. Results concerning the bounds and solutions of the fundamental equation are general, but those concerning instrumental angles depend on the type of diffractometer and the choice of the reference systems; if other settings are used, the general scheme will be the same but particular formulas will differ. For an easy comparison, we follow Kumar et al. [10] in respect of instrumental angles, reference systems, nomenclature and most of notation. It is assumed that measurements are carried out using a perfectly aligned diffractometer and a particular reflection with a fixed Bragg angle (i.e., the search for the peak position is ignored). Angles are considered modulo 2π unless explicit bounds are given, and angle units are radians except in figures where angles are in degrees.

---

[1] Or Ψ and Ω modes [7] or "side-inclination" and "iso-inclination" methods [8], respectively.

2. Penetration depth

Intensity of X-rays passing through a distance p in a material decreases from the initial I_0 to $I_0 \exp(-\mu p)$, where μ is the linear attenuation coefficient. If a measured material property, say strain ϵ, varies along the distance z from the specimen surface, the recorded value ϵ_{rec} is a weighted average of $\epsilon(z)$

$$\epsilon_{rec} = \frac{1}{N} \int_0^\infty \epsilon(z) \exp(-\mu p) \; \mathrm{d}z \; , \tag{1}$$

where $N = \int_0^\infty \exp(-\mu p) \, dz$, and p depends on the measurement geometry, in particular on the distance z; see, e.g., [13, 14]. Diffraction geometry is governed by the Laue equation $\boldsymbol{k} - \boldsymbol{k}_0 = \boldsymbol{h}$, where $\boldsymbol{h}$ is a vector of the reciprocal crystal lattice, $\boldsymbol{k}_0$ and $\boldsymbol{k}$ denote wave vectors of the incident and diffracted beams, and the wave vectors are of equal magnitudes $|\boldsymbol{k}_0| = 1/\lambda = |\boldsymbol{k}|$. The Laue equation can be written as $\boldsymbol{\kappa} + \boldsymbol{\kappa}_0 = \lambda \boldsymbol{h}$, where $\boldsymbol{\kappa} = \lambda \boldsymbol{k}$ and $\boldsymbol{\kappa}_0 = -\lambda \boldsymbol{k}_0$ are unit vectors. With the point of diffraction at $\boldsymbol{0}$, the lines along the beams have parametric equations $\boldsymbol{x} = l_0 \boldsymbol{\kappa}_0$ and $\boldsymbol{x} = l\boldsymbol{\kappa}$, respectively; see Fig. 1. The equation of the specimen surface is $\boldsymbol{n} \cdot \boldsymbol{x} = z$, where $\boldsymbol{n}$ denotes the unit vector normal to the surface. Hence, the intersections of the lines and the surface correspond to parameters l_0 and l given by $l_0 \boldsymbol{n} \cdot \boldsymbol{\kappa}_0 = z$ and $l\boldsymbol{n} \cdot \boldsymbol{\kappa} = z$, and the path of the beams in the material equals $p = l_0 + l = z \left((\boldsymbol{n} \cdot \boldsymbol{\kappa}_0)^{-1} + (\boldsymbol{n} \cdot \boldsymbol{\kappa})^{-1} \right)$. Thus, the weighting distribution $N^{-1} \exp(-\mu p)$ in eq.(1) can be expressed as $\tau^{-1} \exp(-z/\tau)$, where the effective penetration depth τ is linked to geometric parameters $\boldsymbol{\kappa}_0$, $\boldsymbol{\kappa}$ and $\boldsymbol{n}$ via

Fig.1

$$\frac{1}{\mu\tau} = \frac{1}{\boldsymbol{n} \cdot \boldsymbol{\kappa}_0} + \frac{1}{\boldsymbol{n} \cdot \boldsymbol{\kappa}} \; . \tag{2}$$

Equation (2) is fundamental for the description of the strain measurement at a given penetration depth. Since $\boldsymbol{n} \cdot \boldsymbol{\kappa}_0 = \sin \alpha_0$ and $\boldsymbol{n} \cdot \boldsymbol{\kappa} = \sin \alpha$, where α_0 and α are the angles between the specimen surface and the incident and diffracted beams, it is usually written in the form $(\mu\tau)^{-1} = \csc \alpha_0 + \csc \alpha$; cf. [2].

Three remarks concerning the fundamental equation (2) are in place. First, it implies that τ must satisfy the condition

$$2\mu\tau < 1 \; ;$$

surprisingly, this basic inequality is ignored in literature. Second, relationships which follow from eq.(2) involve μ and τ only in the product $\mu\tau$. In other words, measurement geometry is influenced by τ only via $\mu\tau$, and the penetration depth will appear below only in this form. Third, for given $\boldsymbol{\kappa}_0$ and $\boldsymbol{\kappa}$, solutions to eq.(2) must be symmetric with respect to the exchange of these vectors. The experimental configurations related by this exchange will be referred to as coupled configurations.

The central problem addressed in this paper can be formulated as follows: given a value of $\mu\tau$ and a direction of the scattering vector $\boldsymbol{h}$ with respect to the specimen, what are the specimen orientations for which the fundamental equation is satisfied, and what are the goniometer angles corresponding to these orientations. To approach the problem, one needs to specify reference systems and bounds on geometric parameters used for describing it. The

3

analysis begins with getting relations between Cartesian components of $\boldsymbol{n}$ in a laboratory reference system. They lead to explicit bounds on accessibility of the polar angle of $\boldsymbol{n}$ in this system. Subsequently, the link between the components in the laboratory and specimen reference systems is given, and formulas for the goniometer angles are derived.

3. Surface normal in laboratory coordinate system and accessibility bounds

Let the orthonormal laboratory reference system be defined by the basis vectors

$$\boldsymbol{e}_1 = \frac{\boldsymbol{\kappa}_0 - \boldsymbol{\kappa}}{|\boldsymbol{\kappa}_0 - \boldsymbol{\kappa}|} \ , \quad \boldsymbol{e}_2 = \frac{\boldsymbol{\kappa} \times \boldsymbol{\kappa}_0}{|\boldsymbol{\kappa} \times \boldsymbol{\kappa}_0|} \ , \quad \boldsymbol{e}_3 = \frac{\boldsymbol{\kappa}_0 + \boldsymbol{\kappa}}{|\boldsymbol{\kappa}_0 + \boldsymbol{\kappa}|} \ .$$

Vectors $\boldsymbol{e}_1$ and $\boldsymbol{e}_3$ are in the scattering plane, and $\boldsymbol{e}_3$ is along the scattering vector $\boldsymbol{h}$; see Fig. 2. The vector $\boldsymbol{n}$ normal to the specimen surface can be expressed in the laboratory coordinate system as

Fig.2

$$\boldsymbol{n} = \frac{\nu_-}{\sqrt{t_-}} \, \boldsymbol{e}_1 \, + \, n_2 \, \boldsymbol{e}_2 \, + \, \frac{\nu_+}{\sqrt{t_+}} \, \boldsymbol{e}_3 \ ,$$

where $t_+ = |\boldsymbol{\kappa}_0 + \boldsymbol{\kappa}|^2 / 4$ and $t_- = |\boldsymbol{\kappa} - \boldsymbol{\kappa}_0|^2 / 4 = 1 - t_+$. The indices are '$-$' and '$+$' to accent the link of respective parameters to $\boldsymbol{\kappa}_0 - \boldsymbol{\kappa}$ and $\boldsymbol{\kappa}_0 + \boldsymbol{\kappa}$. With such $\boldsymbol{n}$, its scalar products with $\boldsymbol{\kappa}_0$ and $\boldsymbol{\kappa}$ take simple forms

$$\boldsymbol{n} \cdot \boldsymbol{\kappa}_0 = \nu_+ + \nu_- \quad \text{and} \quad \boldsymbol{n} \cdot \boldsymbol{\kappa} = \nu_+ - \nu_- \ . \tag{3}$$

This means that the configuration is symmetric, in the sense that $\boldsymbol{\kappa}_0$ and $\boldsymbol{\kappa}$ are at the same angle to the specimen surface, only if $\nu_- = 0$. Substitution of $\boldsymbol{n} \cdot \boldsymbol{\kappa}_0$ and $\boldsymbol{n} \cdot \boldsymbol{\kappa}$ in eq.(2) leads to

$$\nu_-^2 = \nu_+(\nu_+ - 2\,\mu\tau) \ , \tag{4}$$

and the normalization condition $\boldsymbol{n} \cdot \boldsymbol{n} = 1$ gives an expression for squared n_2

$$n_2^2 = 1 - \nu_+ \frac{\nu_+ - 2\mu\tau\, t_+}{t_+ t_-} \ . \tag{5}$$

Thus, for given diffraction geometry ($\boldsymbol{\kappa}_0$ and $\boldsymbol{\kappa}$) and a given $\mu\tau$, the squared ν_- and n_2 are determined by the parameter ν_+. Besides ν_+, only the signs of ν_- and n_2 remain indefinite.

Accessibility bounds

Since both the incident and diffracted beams must be properly directed with respect to specimen surface, the values of $\boldsymbol{n} \cdot \boldsymbol{\kappa}_0$, $\boldsymbol{n} \cdot \boldsymbol{\kappa}$ and $\boldsymbol{n} \cdot \boldsymbol{e}_3$ must be larger than zero. The condition $\boldsymbol{n} \cdot \boldsymbol{e}_3 > 0$ implies that ν_+ must be positive. The inequalities $\boldsymbol{n} \cdot \boldsymbol{\kappa}_0 > 0$ and $\boldsymbol{n} \cdot \boldsymbol{\kappa} > 0$ do not increase constrains on ν_+ because, based on eqs.(3), they give $|\nu_-| < \nu_+$ which is contained in eq.(4),[2] and the tightest bounds on the free parameter ν_+ follow from the conditions

$$0 \le \nu_-^2 \quad \text{and} \quad 0 \le n_2^2 \ . \tag{6}$$

---

[2]This noteworthy fact has simple interpretation: the requirement of physically sensible penetration depth implies that both beams have attainable directions. Jumping ahead, this means that for arbitrary Bragg angles and for all penetration depths reachable with these Bragg angles, paths of $\boldsymbol{\kappa}_0$ and $\boldsymbol{\kappa}$ in Fig. 4a are confined to the upper hemisphere.

Using eqs. (4) and (5), one gets

$$2\mu\tau \;\leq\; \nu_+ \;\leq\; \mu\tau t_+ + \sqrt{(\mu\tau t_+)^2 + t_- t_+} \; . \tag{7}$$

If ν_+ is at the left bound, then $\nu_- = 0$, i.e., this bound is reached at the aforementioned symmetric configuration (similar to the experimental "χ mode"). At the right bound, one has $n_2 = 0$ and the extreme asymmetric configuration (as in the "ω mode"). The upper bound is larger than the lower bound only if

$$2\mu\tau < \sqrt{t_+} \; ; \tag{8}$$

this is the basic requirement for performing a measurement at a given penetration depth. Its violation means that the considered depth cannot be reached.

Bounds on polar angle ψ

The above conditions can be expressed via standardly used angles. With $\theta = \arcsin(\lambda\,|\boldsymbol{h}|\,/2)$ denoting the Bragg angle ($0 < \theta < \pi/2$), one has $\boldsymbol{\kappa}_0 = \sin\theta\,\boldsymbol{e}_3 + \cos\theta\,\boldsymbol{e}_1$ and $\boldsymbol{\kappa} = \sin\theta\,\boldsymbol{e}_3 - \cos\theta\,\boldsymbol{e}_1$, and hence

$$t_+ = \sin^2\theta \quad\text{and}\quad t_- = \cos^2\theta \; .$$

The requirement (8) implies that $2\mu\tau$ must be smaller than the sine of the Bragg angle

$$2\mu\tau < \sin\theta \; . \tag{9}$$

Let ψ ($0 \leq \psi < \pi/2$) and φ denote, respectively, the polar and the azimuth angles of $\boldsymbol{e}_3$ in the Cartesian specimen coordinate system based on unit vectors $\boldsymbol{s}_1$, $\boldsymbol{s}_2$ and $\boldsymbol{s}_3 = \boldsymbol{n}$. By the definition of ψ, one has $\cos\psi = \boldsymbol{n}\cdot\boldsymbol{e}_3 = \nu_+/\sqrt{t_+}$. Hence,

$$\nu_+ = \sin\theta\cos\psi \; , \tag{10}$$

i.e., the parameter ν_+ is independent of $\mu\tau$, and – for a given Bragg angle – it is directly linked to the polar angle ψ. Substitution of (10) to inequalities (7) gives bounds on admissible values of ψ

$$\cos\psi_{\max} = 2\mu\tau\,\csc\theta \;\leq\; \cos\psi \;\leq\; \left(\mu\tau + \sqrt{(\mu\tau)^2 + \cot^2\theta}\right)\sin\theta = \cos\psi_{\min} \; . \tag{11}$$

When θ approaches $\pi/2$, both lower and upper bound on $\cos\psi$ approach $2\mu\tau$. On the other hand, if $\sin\theta$ approaches $2\mu\tau$, both bounds on ψ approach 0.[3] Example bounds are presented in Fig. 3. Ranges of admissible ψ were also pictured in [10] and [15] for fixed Bragg angles, but these for fixed $\mu\tau$ shown here are more symmetric and in effect more transparent.

    To get reliable results, strain measurements need to be carried out for a wide scope of parameters. The optimal Bragg angle leading to the largest accessibility ranges are given in

Fig.3

---

[3]Corresponding θ- and $\mu\tau$-dependent bounds on ψ were described by Benediktovitch et al. [15]. The upper bound $\psi_{\max}$ agrees with their result, but the lower bounds are different; one can verify by direct calculation that eq.(13) of [15] for the lower bound is not correct.

Appendix A. Practical aspects of the considered measurement are out of the scope of this paper, but one point directly linked to the measurement geometry needs to be mentioned. In principle, all vectors $\boldsymbol{n}$ with components within the limits (7) are accessible. In practice, in the case of small $\mu\tau$, to avoid refraction and surface roughness effects, and to take into account limited accuracy of instruments, one may request the angles α_0 and α to be larger than a certain limiting value $\alpha_{\min}$. The smallest α_0 and α arise when $\psi = \psi_{\min}$, i.e., in the highly asymmetric case. If $\alpha_{\min}$ is small (say, slightly exceeds the critical angle of total external reflection), and the Bragg angle is near the optimal values (21) or (22), then to have α_0 and α larger than $\alpha_{\min}$, the parameter $\mu\tau$ must be larger than $\sin\alpha_{\min} \approx \alpha_{\min}$.

4. Specimen orientations

As was already indicated, the crucial question one faces when working in the "combined ω/χ mode" concerns the specimen orientations in the laboratory reference frame which would lead to a given direction (ψ, φ) of the scattering vector and the desired penetration depth. The special orthogonal matrix, say O, representing the specimen orientation in the laboratory reference frame is built of the direction cosines $O_{ij} = \boldsymbol{s}_i \cdot \boldsymbol{e}_j$, and thus can be written in the form

$$
\begin{array}{c|ccc}
 & \boldsymbol{e}_1 & \boldsymbol{e}_2 & \boldsymbol{e}_3 \\
\hline
\boldsymbol{s}_1 & \cdot & \cdot & \sin\psi\cos\varphi \\
\boldsymbol{s}_2 & \cdot & \cdot & \sin\psi\sin\varphi \\
\boldsymbol{n} = \boldsymbol{s}_3 & \nu_-/\sqrt{t_-} & n_2 & \nu_+/\sqrt{t_+} \ (= \cos\psi)
\end{array} \quad . \tag{12}
$$

Knowing the third column and the last row of O, based on the orthogonality condition $O^{-1} = O^T$ and $\det O = +1$, one can determine the remaining entries, and the result is unique in almost all cases. Taking into account that ν_+ determines the magnitudes of ν_- and n_2 but not their signs, there are in general four[4] distinct configurations with the same ν_+, i.e., with the same orientation of the scattering vector with respect to the specimen. If one of them has parameters (ν_-, n_2, ν_+), the other correspond to $(-\nu_-, -n_2, \nu_+)$, $(-\nu_-, n_2, \nu_+)$ and $(\nu_-, -n_2, \nu_+)$. If one of these solutions is attainable, so are the other three.

The four types of configurations can be pictured in the mind by considering specimen rotations about the scattering vector $\boldsymbol{h} \parallel \boldsymbol{e}_3$. The polar angle of $\boldsymbol{n}$ in the laboratory coordinate system with the polar axis along $\boldsymbol{e}_3$ is ψ. With η denoting the azimuth angle of $\boldsymbol{n}$ in the same system, one has

$$
\nu_-/\sqrt{t_-} = \sin\psi\cos\eta \quad \text{and} \quad n_2 = \sin\psi\sin\eta \ . \tag{13}
$$

To keep the penetration depth constant with the change of ψ, the specimen must also rotate about the scattering vector. One can easily verify that with ψ varying from $\psi_{\min}$ to $\psi_{\max}$, the angle η changes by $\pi/2$. At $\psi = \psi_{\min}$ (the highest asymmetry, $n_2 = 0$), η equals 0 or π, and it equals $\pi/2$ or $3\pi/2$ at $\psi = \psi_{\max}$ (symmetric case, $\nu_- = 0$). For ψ satisfying $\psi_{\min} < \psi < \psi_{\max}$, there are four different values of η leading to the same ν_-^2 and n_2^2. With

---

[4]Solutions overlap when $\nu_- = 0$ or $n_2 = 0$, but their properties in these instances follow from the general case, and therefore, they will not be discussed separately.

one of these values being η, the other three are $\pi - \eta$, $\pi + \eta$ and $2\pi - \eta$. In the standard measurement strategy with variable ψ and constant φ, all possible configurations can be covered by continuous change of η from 0 to 2π and the full range of ψ traversed four times. This is illustrated in Fig. 4. All four stages (numbered 1 to 4) of the complete cycle of η are shown in both sample and laboratory reference frames.

Fig.4

Two orientations linked by the simultaneous change of the signs of both ν_- and n_2 are related by half-turns about $\boldsymbol{e}_3$ and by the exchange of $\boldsymbol{\kappa}_0$ and $\boldsymbol{\kappa}$, i.e., they correspond to coupled configurations. Clearly, there are two pairs of coupled configurations. Since $\sin \alpha_0 = \boldsymbol{n} \cdot \boldsymbol{\kappa}_0 = \nu_+ + \nu_-$ is independent of n_2, among the four types of solutions only two different incidence angles α_0 are possible, and an analogous statement applies to the exit angle α.

5. Goniometer angles

To perform a measurement at a given penetration depth, one needs to link the parameters ψ, φ and $\mu\tau$ to angles of a goniometer. For a detailed description of the angles ω, χ and ϕ of a laboratory four-circle diffractometer the reader is referred to, e.g., [2, 10]. For simplicity, we use $\Omega = \omega - \theta$ instead of ω. Below, the directions of rotations by goniometer angles are selected to match the sign convention used by Kumar et al. [10]. The rotations are schematically illustrated in Fig. 2. With prime and double-prime symbols indicating rotated axes, the orientation of the specimen is determined by composition of the rotation by Ω about $\boldsymbol{e}_2$, the rotation by χ about $\boldsymbol{e}_1'$, and the rotation by ϕ about $-\boldsymbol{e}_3''$.[5] The composition is represented by the matrix

$$
\begin{bmatrix}
\cdot & \cdot & -\sin\phi\sin\chi\cos\Omega - \cos\phi\sin\Omega \\
\cdot & \cdot & \cos\phi\sin\chi\cos\Omega - \sin\phi\sin\Omega \\
\cos\chi\sin\Omega & -\sin\chi & \cos\chi\cos\Omega
\end{bmatrix} ; \tag{14}
$$

see Appendix B. The goniometer angles are obtained by comparing entries of the matrices (12) and (14). At first, to keep formulas reasonably simple, they are listed hierarchically, i.e., preceding equations are needed to calculate a given instrumental angle. Since $|\chi| < \pi/2$, the single expression

$$
\sin\chi = -n_2 \tag{15}
$$

determines the angle χ. Similarly, since $|\Omega| < \pi/2$, the angle Ω is given by the second of the relationships

$$
(\cos\Omega, \ \sin\Omega) = \frac{1}{\sqrt{1 - n_2^2}} \left(\frac{\nu_+}{\sqrt{t_+}}, \ \frac{\nu_-}{\sqrt{t_-}} \right) . \tag{16}
$$

The first one is listed because it can be used for calculating ϕ. The comparison of the entries 13 and 23 of the above matrices leads to

$$
(\cos(\phi - \varphi), \sin(\phi - \varphi)) = - (\sin\Omega, \ \cos\Omega \sin\chi) \csc\psi , \tag{17}
$$

---

[5]The last rotation has the axis direction opposite to $\boldsymbol{e}_3''$ in order to have the same monotonicity of ϕ as that of φ; the angle φ is a magnitude of *active* rotation of the vector $\boldsymbol{e}_3$ about $\boldsymbol{n} = \boldsymbol{s}_3 = \boldsymbol{e}_3''$, whereas ϕ is the angle of *passive* rotation of reference frame about its third axis $\boldsymbol{e}_3''$.

where χ and Ω are given by eqs. (15) and (16), respectively; since the range of ϕ is 2π, both parts of (17) are needed to get the right angle. Using eqs.(15–17) and eqs.(4,5,10) for the components of $\boldsymbol{n}$, one can get the instrumental angles Ω, χ and ϕ explicitly expressed via ψ, φ and $\mu\tau$.

Clearly, the signs of n_2 and ν_- determine the signs of the angles χ and Ω, respectively. Given a configuration described by (Ω, χ, ϕ), the coupled configuration corresponds to the angles $(-\Omega, -\chi, \phi + \pi)$, and the other two configurations with the same ψ and φ are $(\Omega, -\chi, 2\varphi - \phi)$ and $(-\Omega, \chi, 2\varphi - \phi + \pi)$. Since $\cos\psi = \cos\chi\cos\Omega$, one has $\cos\psi \leq \cos\chi$ and $\cos\psi \leq \cos\Omega$, and in consequence $|\chi| \leq \psi$ and $|\Omega| \leq \psi$. The last inequality is weaker than the actual bound on $|\Omega|$; it can be shown that $|\Omega| \leq \psi_{\min}$. For constant φ and the polar angle ψ growing from $\psi_{\min}$ to $\psi_{\max}$, the angle $|\Omega|$ decreases from $\psi_{\min}$ to 0, $|\chi|$ grows from 0 to $\psi_{\max}$, and ϕ alters by $\pi/2$. Example changes of Ω, χ and ϕ needed to cover all configurations in the case with varying ψ and constant φ are shown in Fig. 5. Worth noting is the continuity of the changes.   Fig.5

Relationships involving the angle η

The parameter $\mu\tau$ appears naturally in the description of measurements with controlled penetration depth. However, since a given triplet $(\psi, \varphi, \mu\tau)$ corresponds to multiple specimen orientations, it is convenient to replace $\mu\tau$ by η, as specimen orientations are unambiguously determined by (ψ, η, φ). Based on eqs. (15–17) and (13), it is easy to link (ψ, η, φ) to (Ω, χ, ϕ). With ψ, $|\Omega|$ and $|\chi|$ in the range from 0 to $\pi/2$, the goniometer angles are given by

$$
\begin{aligned}
\Omega &= \arctan\left(\tan\psi\cos\eta\right)\\
\chi &= -\arcsin\left(\sin\psi\sin\eta\right)\\
\phi &= \varphi + \mathrm{atan2}\left(-\cos\eta,\ \cos\psi\sin\eta\right)\ ,
\end{aligned}
\tag{18}
$$

and the inverse relationships are

$$
\begin{aligned}
\psi &= \arccos\left(\cos\chi\cos\Omega\right)\\
\eta &= \mathrm{atan2}\left(\sin\Omega\cos\chi, -\sin\chi\right)\\
\varphi &= \phi + \mathrm{atan2}\left(-\sin\Omega,\ \cos\Omega\sin\chi\right)\ ;
\end{aligned}
\tag{19}
$$

cf. [12]. Eqs. (19) fail if $\Omega = 0 = \chi$, i.e., if $\psi = 0$; this is consistent with the fact that φ and η are undefined at $\psi = 0$. The parameter $\mu\tau$ can be calculated from (ψ, η, φ) or (Ω, χ, ϕ) using

$$
\mu\tau = \frac{\nu_+^2 - \nu_-^2}{2\nu_+} = \frac{\sin^2\theta - \sin^2\psi + \cos^2\theta\sin^2\psi\sin^2\eta}{2\sin\theta\cos\psi} = \frac{\cos\chi\left(\cos^2\Omega - \cos^2\theta\right)}{2\sin\theta\cos\Omega}\ .
\tag{20}
$$

The formula expressing $\mu\tau$ via (ψ, η, φ) is a basis of the so-called "scattering vector method" of z–resolved strain determination [16].

Other accounts on instrumental angles

How does the above formalism relate to previously published formulas? Using the expressions listed above, all instrumental angles, including Ω, can be calculated directly from the measurement parameters $\mu\tau$, ψ and φ. In [10], there is no explicit formula for $\omega = \theta + \Omega$,

and this angle is calculated by numerically solving a variant of eq.(20). The same approach was used in [17]. It has been even claimed that this equation is not explicitly solvable with respect to ω [11]; eq.(16) proves this assertion to be false.

Then there is the issue of the instrumental angle ϕ. Eq.(17) implies that $\tan(\phi - \varphi) = \sin\chi\cot\Omega$. To calculate ϕ, Kumar et al. [10] use the related formula $\phi = \varphi + \arctan(\sin\chi\cot\Omega)$, which gives only angles ϕ differing from φ by less than $\pi/2$, and it fails to give solutions for which $|\phi - \varphi|$ exceeds $\pi/2$. This difficulty is caused by inadequate specification of domains of particular angles. A related issue concerns the first of relationships (19): it is sometimes written simply as $\cos\psi = \cos\chi\cos\Omega$ [10, 11, 17], but sometimes – to avoid an inconsistency referred to in [12] as "a 'flip-flop' phenomenon" – the angle ψ is modified by factor $\mathrm{sgn}(\Omega)$ [2, 12]. There are no such inconsistencies in the formulas listed above.

Finally, eqs. (19) and (20) are similar to corresponding formulas of Francois [12]. The two sets of relationships linking (ψ, η, φ) to (Ω, χ, ϕ) and vice versa in [12] are mutually inverse, on one hand, only if his η is in the range from 0 to $\pi/2$, and on the other, only if Ω and χ have the same signs. Eqs. (19) and (20) are mutually inverse for all experimentally attainable angles.

6. Final remarks

X-ray based measurement of residual strain at chosen penetration depth requires flawless control of all angles of a four-circle diffractometer. This paper addressed a number of issues essential for understanding the geometry of this technique. In particular, accessibility bounds for used angles were given, and a complete solution of the fundamental equation was presented. In general, there are four different specimen orientations for a given penetration depth and a given direction (ψ, φ) of a scattering vector, and accordingly, there are four sets of instrumental angles leading to these orientations. Analytical formulas for all these angles were provided. Detailed understanding of the measurement geometry can be used for devising better measurement strategies.

Parts of the presented formalism are applicable to other depth-resolved strain determination methods. Clearly, the formalism is directly linked to measurements in the "ω mode", "χ mode" and to the "scattering vector method" of Genzel [16]. The presented formulas can be a basis of general measurement strategies, with strains recorded for a large number of specimen orientations and various penetration depths, and with special attention paid to economy of movements of an Eulerian cradle. For simplicity, only the case of compact (bulk) solids with constant attenuation coefficient μ was considered, but a number of observations contained in this paper can be used in the more complicated problem of layered materials, with z-dependent μ. Finally, some results are also relevant for the geometrically similar technique of determining near-surface crystallographic textures [18–20].

References

[1] I. C. Noyan and J. B. Cohen. *Residual Stress; Measurement by Diffraction and Interpretation.* Springer New York, 1987.

[2] U. Welzel, J. Ligot, P. Lamparter, A.C. Vermeulen, and E. J. Mittemeijer. Stress analysis of polycrystalline thin films and surface regions by X-ray diffraction. *J. Appl. Cryst.*, 38:1–29, 2005.

[3] W. Pfeiffer and M. Rombach. Macroscopic and microscopic residual stresses in ceramics due to contact loading. *Adv. X-ray Anal.*, 41:493–500, 1997.

[4] T. Dümmer, B. Eigenmann, M. Stüber, H. Leiste, D. Löhe, H. Müller, and O. Vöhringer. Depth-resolved X-ray analysis of residual stresses in graded PVD coatings of Ti(C,N). *Z. Metallkd.*, 90:780–787, 1999.

[5] A. Kämpfe, B. Eigenmann, and D. Löhe. Comparative application of measuring techniques for X-ray analysis of grinding residual stresses in Al2O3 and AlN. *Z. Metallkd.*, 91:967–975, 2000.

[6] P. Angerer and S. Strobl. Equi-penetration grazing incidence x-ray diffraction method: Stress depth profiling of ground silicon nitride. *Acta Mater.*, 77:370–378, 2014.

[7] H. Ruppersberg, I. Detemple, and J. Krier. $\sigma_{xx}(z)$ and $\sigma_{yy}(z)$ stress-fields calculated from diffraction experiments performed with synchrotron radiation in the Ω- and Ψ-mode techniques. *Z. Kristallogr.*, 195:189–203, 1989.

[8] K. Tanaka and Y. Akiniwa. Diffraction measurements of residual macrostress and microstress using X-rays, synchrotron and neutrons. *JSME Int. J. A-Solid M.*, 47:252–263, 2004.

[9] A. Kumar, U. Welzel, and E. J. Mittemeijer. Depth dependence of elastic grain interaction and mechanical stress: Analysis by x-ray diffraction measurements at fixed penetration/information depths. *J. Appl. Phys.*, 100, 2006.

[10] A. Kumar, U. Welzel, and E. J. Mittemeijer. A method for the non-destructive analysis of gradients of mechanical stresses by X-ray diffraction measurements at fixed penetration/information depths. *J. Appl. Cryst.*, 39:633–646, 2006.

[11] T. Erbacher, A. Wanner, T. Beck, and O. Vöhringer. X-ray diffraction at constant penetration depth a viable approach for characterizing steep residual stress gradients. *J. Appl. Cryst.*, 41:377–385, 2008.

[12] M. François. Unified description for the geometry of X-ray stress analysis: proposal for a consistent approach. *J. Appl. Cryst.*, 41:44–55, 2008.

[13] R. Delhez, Th. H. de Keijser, and E. J. Mittemeijer. Role of x-ray diffraction analysis in surface engineering: Investigation of microstructure of nitrided iron and steels. *Surf. Eng.*, 3:331–342, 1987.

[14] H. Ruppersberg, I. Detemple, and J. Krier. Evaluation of strongly non-linear surface-stress fields $\sigma_{xx}(z)$ and $\sigma_{yy}(z)$ from diffraction experiments. *Phys. Stat. Sol.*, (a) 116:681–687, 1989.

[15] A. Benediktovitch, T. Ulyanenkova, J. Keckes, and Al. Ulyanenkov. Sample tilt-free characterization of residual stress gradients in thin coatings using an in-plane arm-equipped laboratory X-ray diffractometer. *J. Appl. Cryst.*, 47:1931–1938, 2014.

[16] C. Genzel. Formalism for the evaluation of strongly non-linear surface stress fields by X-ray diffraction performed in the scattering vector mode. *Phys. Stat. Sol.*, (a) 146:629–637, 1994.

[17] G. Fischer, U. Selvadurai, J. Nellesen, T. Sprute, and W. Tillmann. Analysis of stress gradients in physical vapour deposition multilayers by X-ray diffraction at fixed depth intervals. *J. Appl. Cryst.*, 47:335–345, 2014.

[18] A. Morawiec. A method of texture inhomogeneity estimation from reflection pole figures. *J. Phys.: Condens. Matter*, 4:339–349, 1992.

[19] J. Bonarski and A. Morawiec. Determination of texture inhomogeneity in near-surface layers. Experimental verification. *J. Appl. Cryst.*, 25:624–627, 1992.

[20] J. T. Bonarski. X-ray texture tomography of near-surface areas. *Progr. Mater. Sci.*, 51:61–149, 2006.

[21] R. A. Winholtz and J. B. Cohen. Generalised Least-squares Determination of Triaxial Stress States by X-ray Diffraction and the Associated Errors. *Aust. J. Phys.*, 41:189–199, 1988.

[22] B. Ortner. Why should we give up the $\sin^2 \psi$ method. *Powder Diffr.*, 24:S16–S21, 2009.

[23] A. Morawiec. *Orientations and Rotations. Computations in Crystallographic Textures.* Springer–Verlag, Berlin, 2004.

Appendix A: The largest accessibility range and the optimal Bragg angle

One is free to choose an arbitrary value of φ. As for ψ, two ways of increasing the scope of the parameters are natural: one may want to have (a) a broad range of ψ, or (b) a large domain of accessible $\boldsymbol{n}$ vectors. The first case is relevant in the standard measurement strategy with variable ψ and constant φ (as in the conventional $\sin^2 \psi$ method), whereas the second one is of importance when the measurement is based on numerous arbitrarily distributed specimen tilts [21, 22].

(a) Fig. $6a$ shows the largest possible $\psi_{\max} - \psi_{\min}$ and the optimal Bragg angle θ at which this range is attained versus $\mu\tau$. The curves were computed numerically, but they are reasonably well approximated by

$$\theta \approx \theta_a = \arcsin\left(2\mu\tau\right)^{1/2} \tag{21}$$

and the corresponding difference $\psi_{\max} - \psi_{\min}$ derived from eq.(11) for $\theta = \theta_a$.

(b) The $\mu\tau$-dependence of the largest fraction $\cos\psi_{\min} - \cos\psi_{\max}$ of the hemisphere covered by accessible $\boldsymbol{n}$ vectors and the Bragg angle at which this fraction is attained are shown in Fig. $6b$. The exact formulas for these curves are relatively complicated, but they can be approximated by

$$\theta \approx \theta_b = \arcsin\left(2\mu\tau\right)^{1/3} \tag{22}$$

and the difference $\cos\psi_{\min} - \cos\psi_{\max}$ for $\theta = \theta_b$.

The functions in Figs. $6a$ and $6b$ are similar but the differences in optimal Bragg angles for the modes (a) and (b) are not negligible; cf. caption of Fig. 3. It is also worth noting that the interpretation of expressions (21) and (22) can be inverted: a given reflection with its Bragg angle θ is most suitable for investigating the material at the depth given by $2\mu\tau \approx \sin^m \theta$, where $m = 2$ in the case (a) and $m = 3$ in the case (b).

Appendix B

A passive rotation of a Cartesian reference frame by an angle ξ about the axis along a unit vector having components $[l_1\, l_2\, l_3]^T$ is represented by a matrix with the entries $\delta_{ij}\cos\xi + l_i l_j(1 - \cos\xi) + \sum_k \varepsilon_{ijk}\, l_k \sin\xi$, $(i, j = 1, 2, 3)$; see, e.g., [23]. With $R_k(\xi)$ denoting the matrix of a rotation about the k-th axis of the Cartesian coordinate system $(k = x, y, z)$, the matrix (14) is equal to the product $R_z(-\phi)\, R_x(\chi)\, R_y(\Omega)$, or explicitly

$$\begin{bmatrix} \cos\phi & -\sin\phi & 0 \\ \sin\phi & \cos\phi & 0 \\ 0 & 0 & 1 \end{bmatrix} \begin{bmatrix} 1 & 0 & 0 \\ 0 & \cos\chi & \sin\chi \\ 0 & -\sin\chi & \cos\chi \end{bmatrix} \begin{bmatrix} \cos\Omega & 0 & -\sin\Omega \\ 0 & 1 & 0 \\ \sin\Omega & 0 & \cos\Omega \end{bmatrix}.$$

Similarly, the matrix (12) can be expressed as

$$R_z(3\pi/2 - \varphi)\, R_x(-\psi)\, R_z(\eta - \pi/2)\ .$$

Thus, eqs. (18–19) linking the triplets (ψ, η, φ) and (Ω, χ, ϕ) can simply be seen as relationships between two different conventions for Euler angles: the classic 'z-x-z' and the unusual 'z-x-y', respectively.
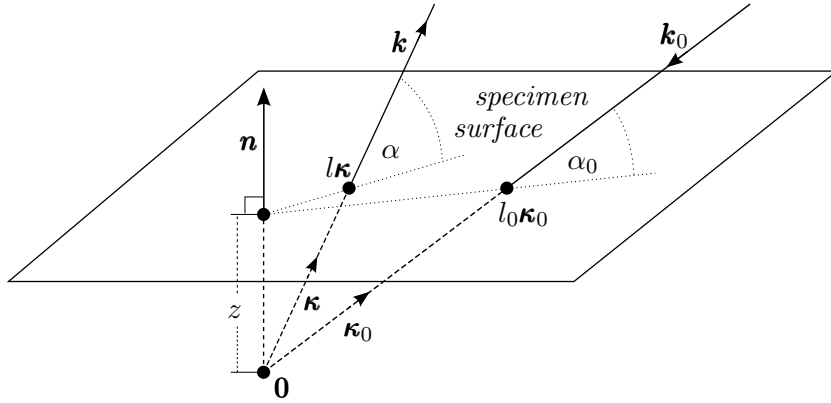
Figure 1: Schematic illustration of entities used for derivation of eq.(2). For the meaning of symbols, see the text.
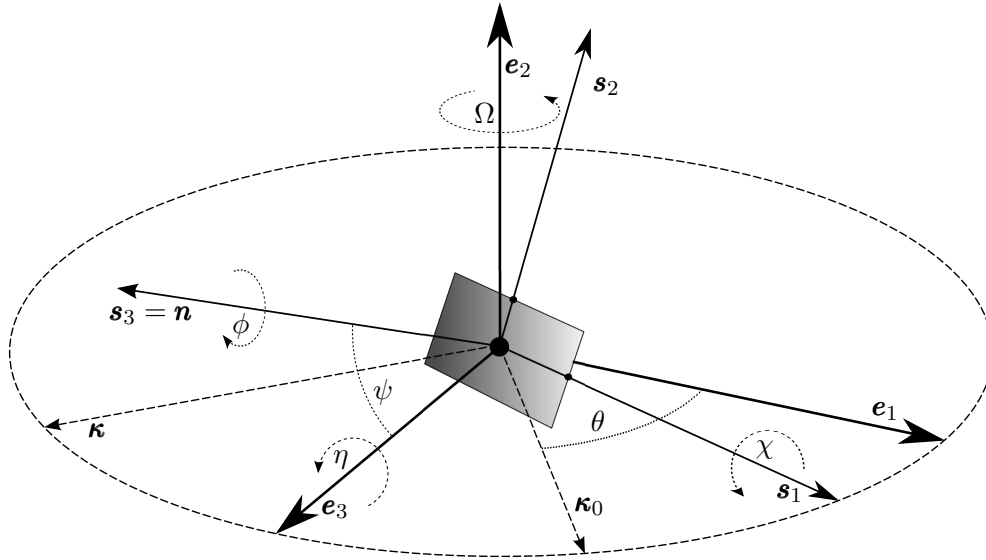
Figure 2: Positions of the laboratory and sample reference systems with respect to the diffraction plane and the beams at $\phi = 0°$ and the adopted directions of goniometer rotations. Vector $\boldsymbol{n}$ is perpendicular to the specimen surface, and $\boldsymbol{e}_3$ is along the scattering vector.
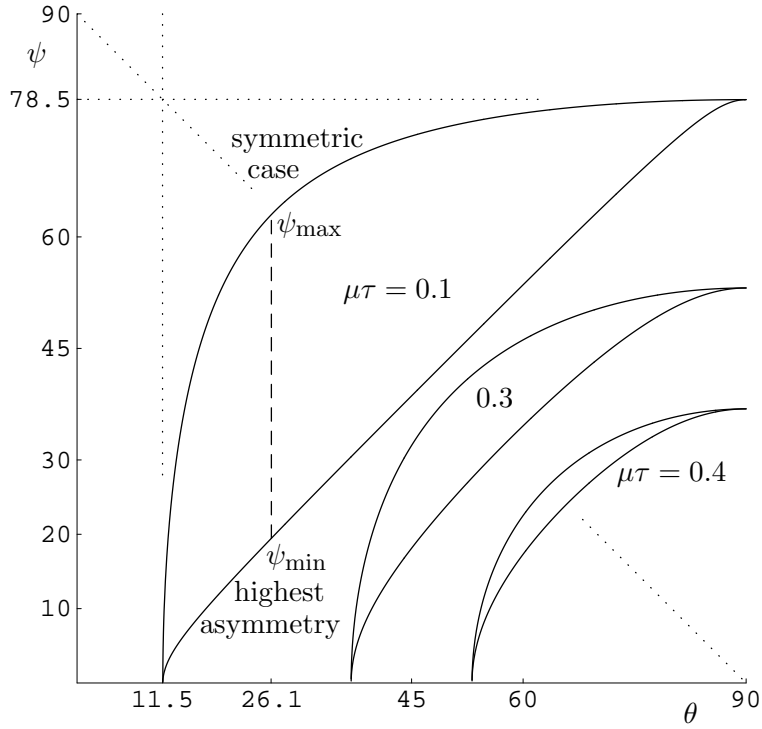
Figure 3: Example accessibility ranges of the angle ψ. Te largest of shown regions corresponds to $\mu\tau = 0.1$. In this case, $\arcsin(2\mu\tau) = 11.5°$ and $\arccos(2\mu\tau) = 90° - 11.5° = 78.5°$. The largest range ($43.5°$) of ψ is reached at $\theta = 26.1°$, whereas the largest domain of accessible $\boldsymbol{n}$ vectors (53% of the hemisphere) is reached at $\theta = 35.3°$. The smaller regions represent the ranges for $\mu\tau = 0.3$ and 0.4. As $\mu\tau$ approaches 0, the region of accessibility approaches the triangle described by $0° < \theta < \psi < 90°$.
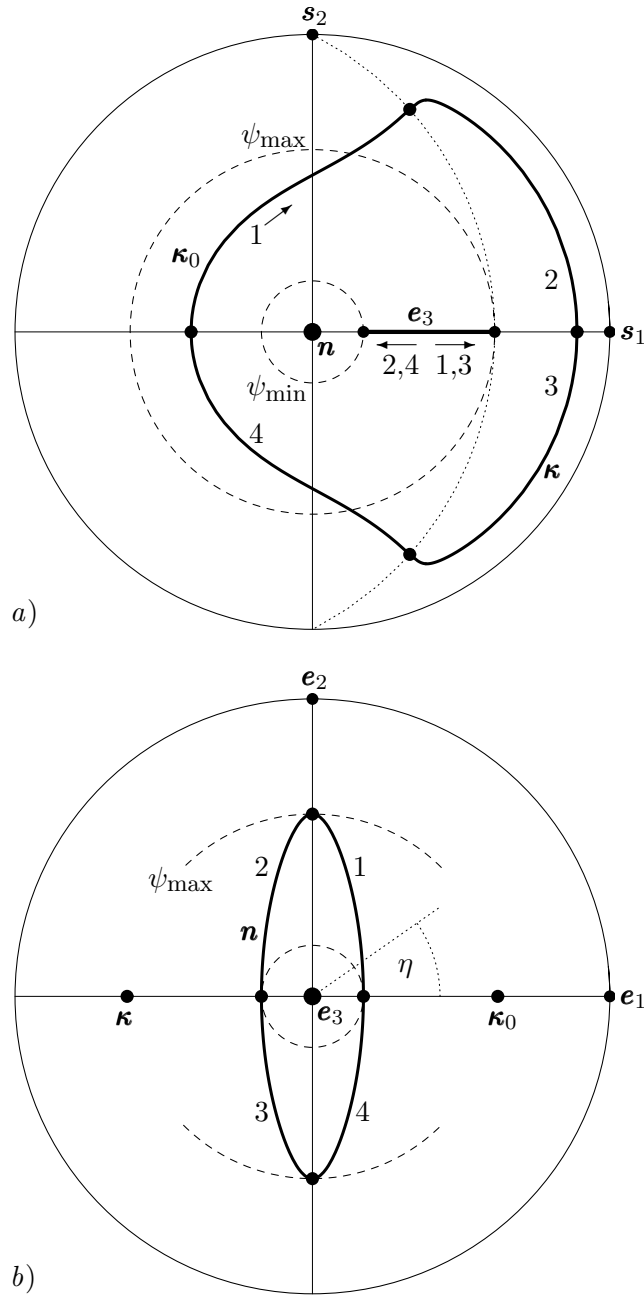
Figure 4: Positions of vectors of interest in the scheme with varying ψ and constant $\varphi = 0°$. a) Stereographic projection of the paths of vectors $\boldsymbol{\kappa}_0$, $\boldsymbol{\kappa}$ and $\boldsymbol{e}_3$ in the specimen reference frame. b) Stereographic projection of the path of vector $\boldsymbol{n}$ in the laboratory reference frame. The numbers indicate locations of $\boldsymbol{\kappa}_0$, $\boldsymbol{n}$ and directions of change of $\boldsymbol{e}_3$ with growing η. The input data are the same as those for the dashed line drawn in Fig. 3, i.e., $\mu\tau$ equals 0.1, the Bragg angle is 26.1°, and ψ varies from $\psi_{\min} \approx 19.5°$ to $\psi_{\max} \approx 63.0°$.
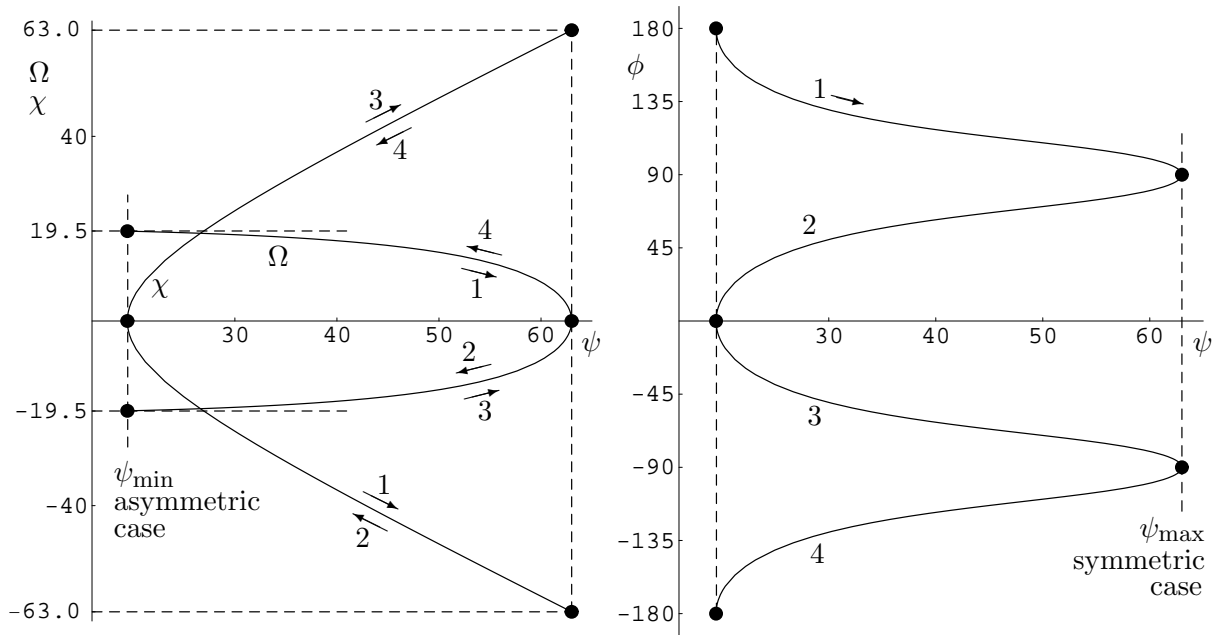
Figure 5: Illustration of variation of the instrumental angles Ω, χ and ϕ versus the polar angle ψ. The input data are the same as those used for drawing Fig. 4. Also the numbering of fragments of the mappings corresponds to that in Fig. 4.
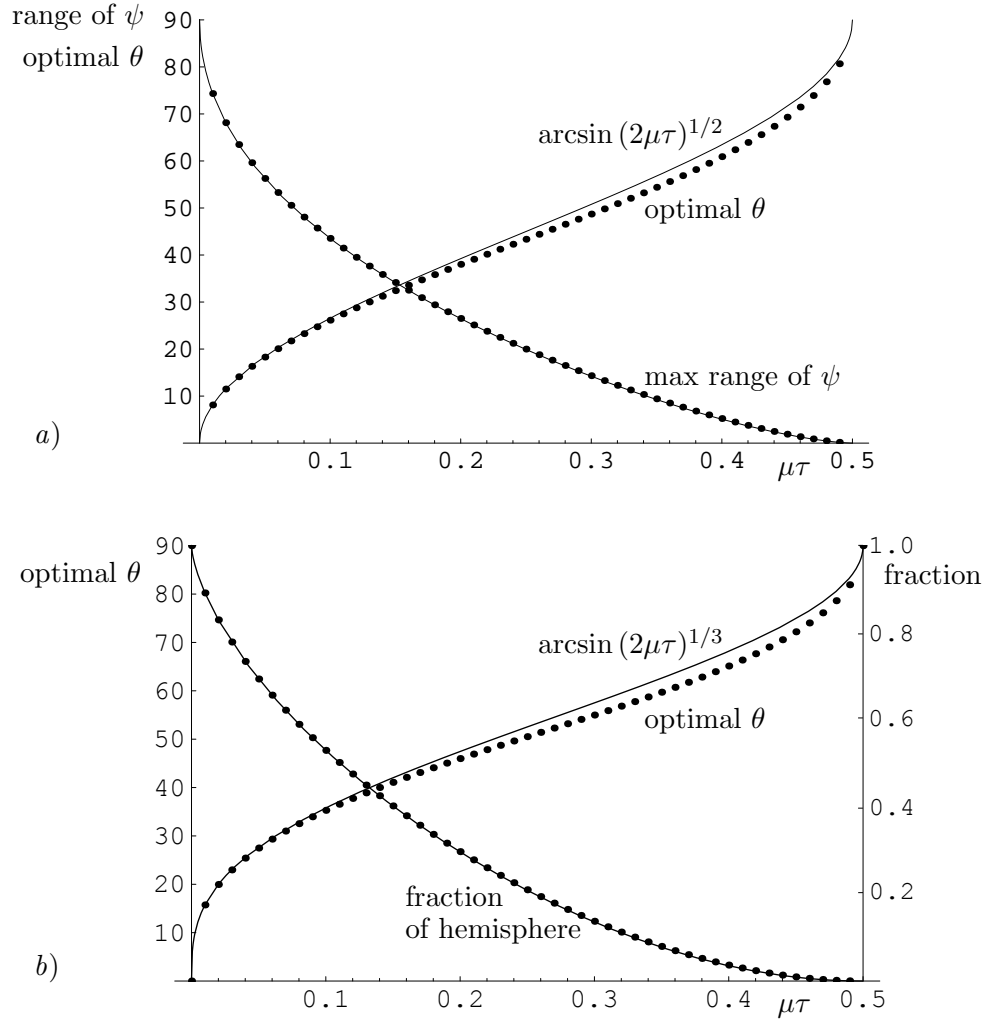
17

Figure 6: *a*) Disks mark numerically estimated Bragg angle θ corresponding to the largest range of ψ for given $\mu\tau$. The continuous curves represent the approximation of the optimal θ by eq.(21) and the corresponding range of ψ obtained from eq.(11). *b*) The Bragg angle θ leading to a largest fraction of the hemisphere covered by accessible vectors $\boldsymbol{n}$ versus $\mu\tau$. The continuous curves represent the approximation of the optimal θ by eq.(22) and the corresponding fraction of the hemisphere obtained from eq.(11).

18